RSC Advances

ROYAL SOCIETY OF CHEMISTRY

www.rsc.org/advances

Graphical Abstract

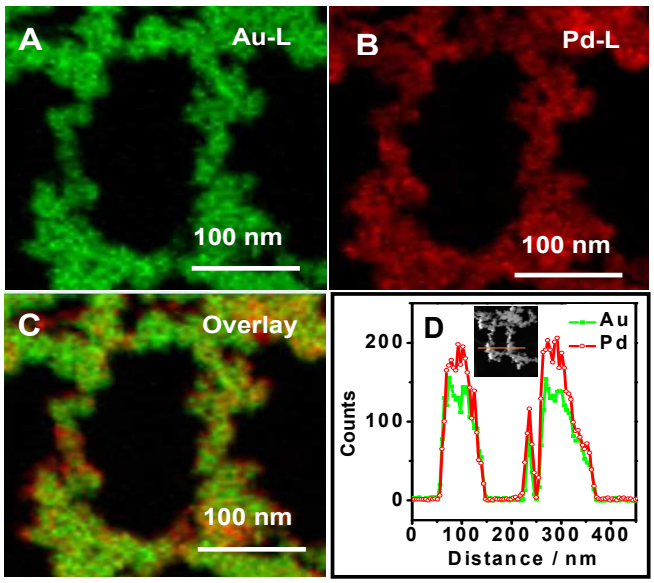

A simple and rapid wet-chemical co-reduction method was developed for synthesis of alloyed Pd-Au nanochains networks supported on RGO, with the assistance of caffeine as a capping agent and a structure directing agent. The as-prepared nanocomposites showed high electrocatalytic activity and stability toward ORR, compared with Pd black and Pd-C catalysts.

Simple synthesis of bimetallic alloyed Pd-Au nanochains networks supported on reduced graphene oxide for enhanced oxygen reduction reaction

Qian-Li Zhang,[a b] Jin-Xia Feng,[b] Ai-Jun Wang,[a] Jie Wei,[a] Jiu-Ju Feng [a] *

[a] *College of Chemistry and Life Science, College of Geography and Environmental Science, Zhejiang Normal University, Jinhua 321004, China*

[b] *School of Chemistry and Biological Engineering, Suzhou University of Science and Technology, Suzhou, 215009, China*

**Corresponding author: jjfeng@zjnu.cn (JJF); Tel./Fax: +86 579 82282269.*

Abstract

Bimetallic alloyed Pd-Au nanochains networks supported on reduced graphene oxide (Pd-Au NNs/RGO) were prepared by a one-pot wet-chemical co-reduction method with the assistance of caffeine as a capping agent and a structure directing agent, while no seed, template, or surfactant was involved. It was found that the dosage of caffeine and the concentrations of the precursors (i.e. $PdCl_4^{2-}$ + $AuCl_4^-$ ions) played essential roles in the formation of Pd-Au NNs. Moreover, the as-prepared nanocomposites exhibited much better electrocatalytic performance than that of conventional Pd black and Pd-C toward oxygen reduction reaction (ORR) in an alkaline media in terms of the onset potential, limiting current, and stability.

Keywords: Reduced graphene oxide; Nanochains networks; Electrocatalysis; Oxygen reduction reaction

1. Introduction

Pt and Pt-based catalysts are generally considered as the most efficient electrocatalysts for oxygen reduction reaction (ORR) in fuel cells, owing to their superior catalytic activity toward direct reduction of oxygen to water via the 4-electron pathway.[1] Unfortunately, these catalysts are seriously inhibited from large-scale commercial applications because of their high cost, limited supply, poor stability, and sluggish kinetics for ORR.[2, 3] Therefore, it is urgent to explore non-Pt catalysts to reduce costs and improve the catalytic activity during ORR. Several good examples are reported in the past, such as Pd,[4] Ir,[5] and Ru-based[6] bimetallic catalysts, oxides,[7, 8] carbide,s[9] and non-precious catalysts.[10-13]

Among various non-Pt catalysts, Pd-based catalysts have attracted great interest as cathode materials in fuel cells, owing to their relatively low cost and more abundance as compared to Pt-based catalysts.[14-17] Particularly, the incorporation of a second metal (M) into Pd (PdM) often brings better catalytic performance, compared to individual counterparts, owing to the synergistic effects and rich diversity of the compositions.[18, 19]

Lately, several PdM catalysts demonstrate the enhanced catalytic activity for ORR, including Pd-Au,[20] Pd-Ni,[21] Pd-Co,[22] Pd-Mo,[23] Pd-Ti,[24] Pd-Ag,[25] and Pd-Cu[26] catalysts. Among them, Pd-Au catalysts have attracted increasing attention for their striking catalytic activity toward ORR.[27-29] For example, Son et al. synthesized sponge-like Pd/Au with higher catalytic activity than single Pd with the similar morphology, commercial Pd-20/C, and Pt-20/C catalysts for ORR.[30] Koenigsmann

and coworkers fabricated Pd_9Au nanowires with superior catalytic performance for oxygen reduction, compared with commercial Pt nanoparticles.[31]

In spite of their enhanced catalytic performances toward ORR, their synthesis is complex, which are usually involved toxic organic solvent, high temperature, time-consuming, sacrificial templates, and complicated synthetic procedures. For instance, Shim and coworkers prepared carbon-supported Pd-coated Au nanoparticles by spontaneous reduction of Pd (II) to Pd on a Au nanoparticles surface, with the reaction time of about ten hours.[20] In another example, Cha' group synthesized carbon-supported porous Pd shell coated Au NNs, using Co nanoframes as sacrificial templates.[28] Therefore, it is of great significance to develop a common, rapid, and environmental friendly approach to fabricate Pd-Au catalysts with the improved electrocatalytic performance.

Given that the catalytic activity of Pd-Au catalysts is not only affected by the morphology, size and dispersion, but also by the nature of a support that is associated with the distribution of the catalysts.[32, 33] Graphene oxide (GO) has abundant oxygen-containing functional groups on the surface (e.g. –OH, –COOH, –C=O), which can be used as anchoring sites for metallic catalysts, along with contributing to its large surface area.[34, 35] Hence, the presence of GO or reduced GO (RGO) is benefit to the catalytic activity of the as-prepared nanocomposites for ORR, as verified by previous work.[36, 37]

Herein, a simple, rapid, and one-pot wet-chemical co-reduction method was explored for synthesis of alloyed Pd-Au nanochains networks uniformly anchored on

reduced graphene oxide (denoted as Pd-Au NNs/RGO), with the assistance of caffeine. The electrocatalytic performance of Pd-Au NNs/RGO was investigated, using ORR as a model system.

2. Experimental

2.1 Chemicals

Graphite powder (99.95%, 8000 mesh), $HAuCl_4$, $PdCl_2$, hydrazine hydrate (80%), caffeine, commercial Pd black and 10% Pd-C were purchased from Shanghai Aladdin Chemical Reagent Company (Shanghai, China). All the other chemicals were of analytical grade and used as received. 1.77 g $PdCl_2$ was dissolved with 0.4 mL HCl (37%), and then diluted to 100 mL with water (100 mM H_2PdCl_4). All solutions were prepared with twice-distilled water throughout the whole experiment.

2.2 Synthesis of Pd-Au NNs/RGO

For typical synthesis of Pd-Au NNs/RGO, GO was firstly prepared from purified natural graphite by a modified Hummer's method.[38] Next, 0.5 mL GO (0.5 mg mL^{-1}) was mixed with 10 mL of aqueous caffeine solution (25 mM) in the ice bath (0 °C), followed by gradual addition of 0.5 mL of 100 mM H_2PdCl_4 and 0.93 mL of 53.95 mM $HAuCl_4$ under stirring. Afterward, 0.2 mL of hydrazine hydrate (80%) was slowly dropped into the mixed solution. The solution color quickly changed from yellow to black, which was further reacted for 15 min. The black precipitate was washed and recollected by consecutive washing/centrifugation cycles with water, and

dried at 60 °C in a vacuum oven for further characterization.

2.3 Characterization

The morphologies and sizes of the samples were characterized by transmission electron microscopy (TEM) and high-resolution TEM (HRTEM) on a JEM-2010HR transmission electron microscope operated at 200 kV equipped with an energy-dispersive X-ray spectrometer (EDS). The samples were prepared by ultrasonic dispersion in ethanol and depositing a drop of the suspension on a copper grid. The crystalline structures were determined by X-ray diffraction (XRD) spectroscopy, which were performed on a Bruker-D8-AXS diffractometer system equipped with Cu Kα radiation (Bruker Co., Germany). The elemental composition analysis was measured by X-ray photoelectron spectroscopy (XPS), which were conducted by a K-Alpha XPS spectrometer (ThermoFisher, E. Grinstead, UK), using Al Kα X-ray radiation (hν = 1486.6 eV). Raman spectra were recorded on a Renishaw Raman system model 1000 spectrometer equipped with a charge coupled device (CCD) detector. Fourier-transform infrared (FT-IR) spectra were recorded on a Nicolet NEXUS-670 FT-IR spectrometer from 500 to 4000 cm^{-1}. Thermogravimetric analysis (TGA, NETZSCH STA 449C) was performed with a heating rate of 10 °C min^{-1} in air atmosphere from room temperature to 800 °C.

2.4 Electrochemical measurements

Electrochemical measurements were carried out on a CHI 660D electrochemical

workstation (CH Instruments, Chenhua Co., Shanghai, China). A conventional three electrode cell was used, including an Ag-AgCl electrode as reference electrode, a platinum wire as counter electrode, and a bare, modified glassy carbon electrode (GCE, 3 mm in diameter) or rotating disk electrode (RDE, 4 mm in diameter) as working electrode.

For fabrication of Pd-Au NNs/RGO modified electrode, 4 mg of Pd-Au NNs/RGO was dispersed in 2 mL water under ultrasonication for 30 min to obtain a homogenous suspension. Then, 8 and 20 μL of the resulting suspension were deposited on the pre-cleaned GCE and RDE, respectively, and allowed to dry in air. After drying, 4 and 10 μL of Nafion (0.05 wt %) were deposited onto the electrode surfaces, respectively. For comparison, Pd-black and Pd-C modified electrodes were prepared in a similar way.

The electrochemically active surface area (ECSA) of the catalysts modified GCE was calculated by the CO stripping experiments. CO gas was firstly adsorbed on the modified GCE at 0.1 V for 900 s in 0.5 M CO-saturated H_2SO_4, and then recorded the corresponding CO-stripping voltammograms in H_2SO_4.

The electrocatalytic performances of the catalysts modified RDE were determined in 0.1 M oxygen-saturated KOH at a scan rate of 5 mV s^{-1} from 100 to 3600 rpm. Meanwhile, the stability tests were conducted in oxygen-saturated 0.1 M KOH at the half-wave potential by chronoamperometry, with a rotating rate of 1600 rpm. All the tests were performed at room temperature, if not sated otherwise.

3. Results and discussion

3.1 Characterization of Pd-Au NNs/RGO

The morphology and size of Pd-Au NNs/RGO were examined by TEM analysis (Fig. 1). As can be seen, the product contains a lot of typical Pd-Au NNs well dispersed on RGO surface (Fig. 1A and B). The absence of caffeine yields heavy aggregated nanoparticles (Fig. S1A, Supplementary Information). Alternatively, excessive caffeine induces the destruction of the network-like structures (e.g. 50 mM, Fig. S1B). Therefore, caffeine is critical for synthesis of Pd-Au NNs, which serves as a capping agent and a structure directing agent to effectively prevent the aggregation of Pd-Au nanocrystals on RGO sheets.[39]

Besides, less (e.g. 1 mM) and excess (e.g. 7.5 mM) amounts of the total precursors (i.e. $PdCl_4^{2-}$ and $AuCl_4^-$) produce seriously aggregated Pd-Au nanoparticles. (Fig. S2, Supplementary Information). These observations imply the essential role of the precursors with appropriate concentrations in the present system.

HRTEM images show good crystallinity of Pd-Au NNs (Fig. 1C and D), as indicated by their well-defined fringe pattern. Moreover, the inter-planar distance between two adjacent fringes is about 0.233 nm, corresponding to the (111) planes of face-centered cubic (fcc) Pd-Au alloy.[40] These observations indicate that the precursors are simultaneously reduced by hydrazine hydrate to form alloy at the very early stage, and the Pd-Au nanocrystals grow along the (111) directions.[41, 42]

Meanwhile, HAADF-STEM-EDS mapping and line scanning profiles were conducted to examine the elemental distributions in Pd-Au NNs. As displayed in Fig.

2, Au and Pd atoms are uniformly distributed across the whole nanochains networks. It means the formation of Pd-Au alloy, rather than the mixture of Pd and Au.

EDS (Fig. 3A) and XRD (Fig. 3B) measurements were carried out to evaluate the composition and crystal structures of Pd-Au NNs/RGO. EDS analysis shows that the content of Au is more abundant than that of Pd in Pd-Au NNs, with Pd to Au at atomic ratio of 1.0: 1.8. The difference is attributed to different reduction potentials of Au^{3+} ($AuCl_4^-$/Au, 1.002 V vs. SHE) and Pd^{2+} ($PdCl_4^{2-}$/ Pd, 0.591 V vs. SHE). Notably, Au^{3+} is more easily reduced, compared with Pd^{2+}, leading to the formation of Au-rich alloys.

Fig. 3B shows the XRD spectrum of Pd-Au NNs/RGO (curve a), in which the representative peak at 38.4° emerges between the diffraction peaks of the Au (111) and Pd (111) crystal planes, confirming the formation of Pd-Au alloy.[43] And a broad peak at 21.2° is assigned to the (002) planes of RGO,[44] which is different from that of GO with a sharp peak at 11.0° (Fig. 3B, curve b), indicating the effective reduction of GO.[45]

XPS is an effective method to investigate elemental composition and valence state of materials. Fig. 4A shows that the peaks located at 532.6, 335.3, 284.5, and 85.1 eV correspond to O 1s, Pd 3d, C 1s, and Au 4f in the survey XPS spectrum, respectively, revealing the presence of Pd and Au in Pd-Au NNs/RGO. In the high-resolution Pd 3d region (Fig. 4B), the binding energies centered at 341.1 eV (Pd $3d_{3/2}$) and 335.6 eV (Pd $3d_{5/2}$), 341.9 eV (Pd $3d_{3/2}$) and 336.5 eV (Pd $3d_{5/2}$) are assigned to metallic Pd^0 and Pd^{2+},[46] respectively. While only one pair of peaks is

emerged at 87.8 and 84.1 eV in the Au 4f region (Fig. 4C), which is ascribed to $4f_{5/2}$ and $4f_{7/2}$ of metallic Au^0,[47] revealing complete reduction of $AuCl_4^-$ in the present synthesis. All these results further confirm that metallic Pd^0 and Au^0 are the predominant species.

For the C 1s XPS spectrum (Fig. 4D), there is a strong peak at 248.7 eV corresponding to the C–C bonds, along with three relatively weaker ones at 286.5, 287.5, and 288.8 eV associated with the C–O, C=O, and O–C=O bonds, respectively.[48, 49] It indicates that GO is reduced to RGO, as strongly supported by the FT-IR and Raman analysis.

As depicted in Fig. 5A, the FT-IR spectrum of Pd-Au NNs/RGO (Fig. 5A, curve a) clearly shows that the characteristic peak of C=O stretching vibration of carboxyl at 1733.5 cm^{-1} and C–O stretching vibration of epoxy and alkoxy at 1058.2 cm^{-1} are weaker, compared with the C=C skeletal vibration at 1663.2 cm^{-1},[50] using the spectrum of GO (Fig. 5A, curve b) as a standard. It reveals the efficient removal of most oxygen containing functional groups.

Meanwhile, as illustrated by Raman spectra (Fig. 5B), the peak intensity ratio of *D* band (the E_{2g} mode of sp^2 carbon atoms) to *G* band (the A_{1g} breathing mode of disordered graphite structure) for Pd-Au NNs/RGO (Fig. 5B, curve a) increases significantly, using the Raman spectrum of GO as a reference (Fig. 5B, curve b). This change suggests the formation of smaller graphene sp^2 domains after the reduction of GO[48] and at the same time confirms the effective reduction of GO to RGO again.

The thermal stability of Pd-Au NNs/RGO was examined by TGA (Fig. S3, curve

a, Supplementary Information)). It is worth noting that there is a slight weight loss below 100 °C for Pd-Au NNs/RGO, which is attributed to the loss of absorbed water molecules on the surface, no obvious weight loss is detected when the sample is further heated up to 800 °C. This phenomenon is quite different from that of GO (Fig. S3, curve b, Supplementary Information)) under the identical conditions, in which GO shows two distinguished drops at 200 and 500 °C corresponding to the decomposition of oxygen-containing functional groups and carbon oxidation,[51] respectively. These results combined with the above analysis further demonstrate the efficient reduction of GO to RGO. Additionally, the load of Pd-Au NNs is about 91 wt % in Pd-Au NNs/RGO.

3.2 Electrochemical measurements

Cyclic voltammetry is a convenient and efficient method to determine the electrochemical activity of a catalyst on an electrode. Fig. S4 (Supplementary Information) provides the typical cyclic voltammograms (CVs) of Pd-Au NNs/RGO (curve a) and Pd-black (curve b) modified electrodes in 0.5 M H_2SO_4. It can be seen that hydrogen adsorption/desorption charges (Q_{Hads}/Q_{Hdes}) of Pd-Au NNs/RGO are higher than those of Pd-black, revealing the enlarged ECSA and more active sites available for Pd-Au NNs/RGO toward ORR.[52]

As known, bulk Pd can absorb hydrogen to form Pd hydride,[53] and hence the ECSA of catalysts were measured by CO stripping experiments. Fig.6 offers the ECSA value of the catalysts, which are obtained by Eq. (1):[54]

$$ECSA = \frac{Q}{m \times 420} \quad (1)$$

where Q is the charge for CO desorption electrooxidation in micro-coulomb (μC), m is the loading amount of Pd (μg), and 420 is the charge required to oxidize a monolayer of CO on metal (μC cm^{-2}). The ECSA value is 28.17 m^2 g^{-1} for Pd-Au NNs/RGO (Fig. 6A), which is much higher than that of Pd-black (1.72 m^2 g^{-1}, Fig. 6B). Additionally, owing to the special nanostructure, the onset potential of CO_{ads} oxidation on Pd-Au NNs/RGO is negatively shifted by about 120 mV in comparison with commercial Pd-black.

To examine the electrocatalytic activity of Pd-Au NNs/RGO, the ORR corresponding polarization curves were recorded in oxygen-saturated 0.1 M KOH, using Pd-black and Pd-C as references. As displayed in Fig. 7A, the onset potential and half-wave potential ($E_{1/2}$) for Pd-Au NNs/RGO (Fig. 7A, curve a) are –0.03 V and –0.13 V toward O_2 reduction, respectively, which are much more positive than those of Pd-black (Fig. 7A, curve b) and Pd-C (Fig. 7A, curve c), highlighting that the NNs structures facilitate ORR more favorably.[55] Therefore, Pd-Au NNs/RGO exhibits much higher diffusion-limiting current density than those of Pd-black and Pd-C. Importantly, the mass activity of Pd-Au NNs/RGO at –0.1 V is found to be the highest among the three catalysts (Fig. 7B). It means that Pd-Au NNs/RGO with the significantly improved catalytic activity toward oxygen reduction.

In order to examine the kinetics of ORR catalyzed by Pd-Au NNs/RGO, a series of polarization curves on Pd-Au NNs/RGO modified electrode were recorded in oxygen-saturated 0.1 M KOH with different rotation rates from 100 to 3600 rpm (Fig.

7C). Evidently, the limiting current densities increase with rotation rates, owing to the enhanced oxygen diffusion.[56] Furthermore, the number of transferred electrons (n) for Pd-Au NNs/RGO is calculated by the below Koutechy-Levich equation:[57, 58]

$$\frac{1}{i} = \frac{1}{i_k} + \frac{1}{i_d} = \frac{1}{i_k} + \frac{1}{B\omega^{1/2}} \quad (2)$$

$$B = 0.2nFC_0D_0^{2/3}\nu^{-1/6} \quad (3)$$

where i_k is the kinetic current, ω is the rotation rate, n is the number of the transferred electrons per oxygen molecule, F is the Faraday constant (96500 C mol^{-1}), C_0 is the oxygen solubility (1.1×10^{-3} mol L^{-1}), D_0 is the diffusion coefficient of oxygen in 0.1 M KOH (1.9×10^{-5} cm^2 s^{-1}), and ν is the kinetic viscosity of the electrolyte (0.01 cm^2 s^{-1}).

As shown in Fig. 7D, the K-L plots (j^{-1} vs. $\omega^{-1/2}$) for Pd-Au NNs/RGO at the potential ranging from −0.15 to −0.25 V exhibit good linearity, suggesting the first-order kinetics relative to the reactant concentration. And the electron transfer number is calculated from the slopes of K–L plots, with the values of 3.91, 3.82, and 3.90 electrons transferred at –0.15 V, –0.2 V, and –0.25 V, respectively, indicating approximate four-electron transfer pathway for Pd-Au NNs/RGO. That is, oxygen is directly reduced to water. The above discussion demonstrates that Pd-Au NNs/RGO is a compelling catalyst for oxygen reduction.

Fig. 8 shows the ORR polarization curves recorded by 1000 times in O_2 saturated 0.1 M KOH on Pd-Au NNs/RGO modified electrode. After the durability test, similar polarization curve was observed in terms of the onset potential, half-wave potential and limiting current, evidencing the improved stability of Pd-Au NNs/RGO. It

demonstrates Pd-Au NNs/RGO with improved stability toward ORR. On the other hand, the stability/durability of Pd-Au NNs/RGO (Fig. 9, curve a) was also evaluated by chronoamperometry, using Pd-black (Fig. 9, curve b) and Pd-C (Fig. 9, curve c) as references. As illustrated in Fig. 9, the corresponding cathode current densities primarily show a gradual decay and then achieve a relatively steady state. Notably, Pd-Au NNs/RGO (Fig. 9, curve a) exhibits considerably higher current and superior stability during the entire process, compared with Pd-black (Fig. 9, curve b) and Pd-C (Fig. 9, curve c). These results demonstrate that Pd-Au NNs/RGO is a stable electrocatalyst for ORR.

Taking the results from both activity and stability studies together, Pd-Au NNs/RGO has the enhanced electrocatalytic performances. This is ascribed to the following features: (I) promotional effects of Au in Pd-Au alloys,[59] (II) synergistic effects between Au and Pd atoms,[60, 61] (III) well-dispersed Pd-Au NNs on RGO with high loading, (IV) unique structures of Pd-Au NNs make the catalyst better stability,[28] and (V) graphene as a support in tuning electrocatalysis for highly efficient ORR.[62]

4. Conclusion

Well-defined bimetallic alloyed Pd-Au NNs were uniformly supported on RGO through one-pot wet-chemical co-reduction method, with the assistance of caffeine as a capping agent and a structure directing agent, which was simple, facile, and straightforward. Pd-Au NNs/RGO exhibited much better electrochemical performance than commercial Pd-black and Pd-C toward ORR in terms of the onset potential,

limiting current, and stability. The prepared Pd-Au NNs/RGO was a very promising cathodic catalyst in fuel cells. The synthetic method described herein can be extended to the preparation of other advanced RGO supported bimetallic catalysts.

Acknowledgments

This work was financially supported by the National Natural Science foundation of China (21475118, 21175218, 21275130, and 51178283), Zhejiang province university young academic leaders of academic climbing project (pd2013055).

References

1. Y. Liu, Y.-Y. Wu, G.-J. Lv, T. Pu, X.-Q. He and L.-L. Cui, *Electrochim. Acta*, 2013, **112**, 269-278.
2. L. Qu, Y. Liu, J.-B. Baek and L. Dai, *ACS Nano*, 2010, **4**, 1321-1326.
3. G. Fu, K. Wu, J. Lin, Y. Tang, Y. Chen, Y. Zhou and T. Lu, *J. Phys. Chem. C*, 2013, **117**, 9826-9834.
4. K. Jukk, N. Alexeyeva, P. Ritslaid, J. Kozlova, V. Sammelselg and K. Tammeveski, *Electrocatalysis*, 2013, **4**, 42-48.
5. J. Qiao, R. Lin, B. Li, J. Ma and J. Liu, *Electrochim. Acta*, 2010, **55**, 8490-8497.
6. V. I. Zaikovskii, K. S. Nagabhushana, V. V. Kriventsov, K. N. Loponov, S. V. Cherepanova, R. I. Kvon, H. Bönnemann, D. I. Kochubey and E. R. Savinova, *J. Phys Chem. B*, 2006, **110**, 6881-6890.
7. K. Suito, A. Ishihara, M. Arao, M. Matsumoto, H. Imai, Y. Kohno, K. Matsuzawa,

S. Mitsushima and K.-I. Ota, *ECS Trans.*, 2013, **50**, 1777-1783.

8. N. Uehara, A. Ishihara, Y. Kohno, K. Matsuzawa, S. Mitsushima and K.-I. Ota, *ECS Trans.*, 2013, **58**, 1217-1223.
9. K. Lee, A. Ishihara, S. Mitsushima, N. Kamiya and K.-I. Ota, *Electrochim. Acta*, 2004, **49**, 3479-3485.
10. Y. Zhang, K. Fugane, T. Mori, L. Niu and J. Ye, *J. Mater. Chem.*, 2012, **22**, 6575-6580.
11. N. Brun, S. A. Wohlgemuth, P. Osiceanu and M. M. Titirici, *Green Chem.*, 2013, **15**, 2514-2524.
12. Z. Schnepp, Y. Zhang, M. J. Hollamby, B. R. Pauw, M. Tanaka, Y. Matsushita and Y. Sakka, *J. Mater. Chem. A*, 2013, **1**, 13576-13581.
13. S. Yasuda, L. Yu, J. Kim and K. Murakoshi, *Chem. Commun.*, 2013, **49**, 9627-9629.
14. S. Takenaka, N. Susuki, H. Miyamoto, E. Tanabe, H. Matsune and M. Kishida, *Chem. Commun.*, 2010, **46**, 8950-8952.
15. J. L. Fernández, V. Raghuveer, A. Manthiram and A. J. Bard, *J. Am. Chem. Soc.*, 2005, **127**, 13100-13101.
16. M.-H. Shao, K. Sasaki and R. R. Adzic, *J. Am. Chem. Soc.*, 2006, **128**, 3526-3527.
17. O. Savadogo, K. Lee, K. Oishi, S. Mitsushima, N. Kamiya and K. I. Ota, *Electrochem. Commun.*, 2004, **6**, 105-109.
18. Y. Zhai, J. Zhai and S. Dong, *Chem. Commun.*, 2010, **46**, 1500-1502.
19. J. Bao, W. Chen, T. Liu, Y. Zhu, P. Jin, L. Wang, J. Liu, Y. Wei and Y. Li, *ACS*

Nano, 2007, **1**, 293-298.

20. J. H. Shim, J. Kim, C. Lee and Y. Lee, *Chem. Mater.*, 2011, **23**, 4694-4700.
21. C. Xu, Y. Liu, Q. Hao and H. Duan, *J. Mater. Chem. A*, 2013, **1**, 13542-13548.
22. R. Rahul, R. Singh and M. Neergat, *J. Electroanal. Chem.*, 2014, **712**, 223-229.
23. C. J. Cao, X. G. Liu and Q. Liu, *Adv. Mater. Res.*, 2013, **785**, 390-394.
24. Y. Liu and C. Xu, *ChemSusChem*, 2013, **6**, 78-84.
25. C.-L. Lee, H.-P. Chiou, C.-M. Syu, C.-R. Liu, C.-C. Yang and C.-C. Syu, *Int. J. Hydrogen Energy*, 2011, **36**, 12706-12714.
26. Y. Sha, T. H. Yu, B. V. Merinov and W. A. Goddard, *ACS Catalysis*, 2014, **4**, 1189-1197.
27. J. S. Jirkovský, I. Panas, S. Romani, E. Ahlberg and D. J. Schiffrin, *J. Phys. Chem. Lett*, 2012, **3**, 315-321.
28. A. Cha, J. H. Shim, A. Jo, S. C. Lee, Y. Lee and C. Lee, *Electroanalysis*, 2014, **26**, 723-731.
29. J.-N. Zheng, S.-S. Li, X. Ma, F.-Y. Chen, A.-J. Wang, J.-R. Chen and J.-J. Feng, *J. Power Sources*, 2014, **262**, 270-278.
30. J. Son, S. Cho, C. Lee, Y. Lee and J. H. Shim, *Langmuir*, 2014, **30**, 3579-3588.
31. C. Koenigsmann, E. Sutter, T. A. Chiesa, R. R. Adzic and S. S. Wong, *Nano Lett.*, 2012, **12**, 2013-2020.
32. T. Maiyalagan and K. Scott, *J. Power Sources*, 2010, **195**, 5246-5251.
33. T. Maiyalagan, X. Wang and A. Manthiram, *RSC Adv.*, 2014, **4**, 4028-4033.
34. X. Huang, X. Qi, F. Boey and H. Zhang, *Chem. Soc. Rev.*, 2012, **41**, 666-686.

35. S. I. Shin, A. Go, I. Y. Kim, J. M. Lee, Y. Lee and S.-J. Hwang, *Energy Environ. Sci.*, 2013, **6**, 608-617.

36. Q.-L. Zhang, T.-Q. Xu, J. Wei, J.-R. Chen, A.-J. Wang and J.-J. Feng, *Electrochim. Acta*, 2013, **112**, 127-132.

37. S. Xu, L. Yong and P. Wu, *ACS Appl. Mat. Interfaces*, 2013, **5**, 654-662.

38. W. S. Hummers Jr and R. E. Offeman, *J. Am. Chem. Soc.*, 1958, **80**, 1339-1339.

39. H.-J. Choi, S.-M. Jung, J.-M. Seo, D. W. Chang, L. Dai and J.-B. Baek, *Nano Energy*, **1**, 534-551.

40. S. C. Y. Tsen, P. A. Crozier and J. Liu, *Ultramicroscopy*, 2003, **98**, 63-72.

41. F. Lan, D. Wang, S. Lu, J. Zhang, D. Liang, S. Peng, Y. Liu and Y. Xiang, *J. Mater. Chem. A*, 2013, **1**, 1548-1552.

42. X. Yu, D. Wang, Q. Peng and Y. Li, *Chem. Eur. J.*, 2013, **19**, 233-239.

43. X. Gu, Z.-H. Lu, H.-L. Jiang, T. Akita and Q. Xu, *J. Am. Chem. Soc.*, 2011, **133**, 11822-11825.

44. T.-Q. Xu, Q.-L. Zhang, J.-N. Zheng, Z.-Y. Lv, J. Wei, A.-J. Wang and J.-J. Feng, *Electrochim. Acta*, 2014, **115**, 109-115.

45. S. Pei, J. Zhao, J. Du, W. Ren and H.-M. Cheng, *Carbon*, 2010, **48**, 4466-4474.

46. Z. Jin, D. Nackashi, W. Lu, C. Kittrell and J. M. Tour, *Chem. Mater.*, 2010, **22**, 5695-5699.

47. H.-G. Boyen, G. Kästle, F. Weigl, B. Koslowski, C. Dietrich, P. Ziemann, J. Spatz, S. Riethmüller, C. Hartmann and M. Möller, *Science*, 2002, **297**, 1533-1536.

48. S. Stankovich, D. A. Dikin, R. D. Piner, K. A. Kohlhaas, A. Kleinhammes, Y. Jia,

Y. Wu, S. T. Nguyen and R. S. Ruoff, *Carbon*, 2007, **45**, 1558-1565.

49. W. Tang, S. Jayaraman, T. F. Jaramillo, G. D. Stucky and E. W. McFarland, *J. Phys. Chem. C*, 2009, **113**, 5014-5024.

50. J. Zhang, H. Yang, G. Shen, P. Cheng, J. Zhang and S. Guo, *Chem. Commun.*, 2010, **46**, 1112-1114.

51. C. Xu, X. Wang, J. Zhu, X. Yang and L. Lu, *J. Mater. Chem.*, 2008, **18**, 5625-5629.

52. X. Xue, C. Bock, L. Birry and B. MacDougall, *Fuel Cells*, 2011, **11**, 286-300.

53. X.-M. Wang and Y.-Y. Xia, *Electrochim. Acta*, 2009, **54**, 7525-7530.

54. Z.-B. Wang, G.-P. Yin, J. Zhang, Y.-C. Sun and P.-F. Shi, *J. Power Sources*, 2006, **160**, 37-43.

55. Y.-B. Cho, J. E. Kim, J. H. Shim, C. Lee and Y. Lee, *Phys. Chem. Chem. Phys.*, 2013, **15**, 11461-11467.

56. Z. Jiang, Z.-j. Jiang, X. Tian and W. Chen, *J. Mater. Chem. A*, 2014, **2**, 441-450.

57. S. Wang, D. Yu, L. Dai, D. W. Chang and J.-B. Baek, *ACS Nano*, 2011, **5**, 6202-6209.

58. S. Wang, D. Yu and L. Dai, *J. Am. Chem. Soc.*, 2011, **133**, 5182-5185.

59. M. Chen, D. Kumar, C.-W. Yi and D. W. Goodman, *Science*, 2005, **310**, 291-293.

60. G. J. Hutchings, *Chem. Commun.*, 2008, 1148-1164.

61. J. W. Hong, M. Kim, Y. Kim and S. W. Han, *Chem. Eur. J.*, 2012, **18**, 16626-16630.

62. S. Guo, S. Zhang, L. Wu and S. Sun, *Angew. Chem.*, 2012, **124**, 11940-11943.

Captions

Fig. 1. Representative low- (A, B) and high- (C, D) resolution TEM images of Pd-Au NNs/RGO.

Fig. 2. HAADF-STEM-EDS mapping (A, B, C) and EDS line scanning profiles (D) of an individual Pd-Au NN.

Fig. 3. (A) EDS pattern of Pd-Au NNs/RGO. (B) XRD patterns of Pd-Au NNs/RGO (curve a), GO (curve b), and the standard patterns of bulk Pd and Au.

Fig. 4. Survey (A), and high-resolution Pd 3d (B), Au 4f (C), and C 1s (D) XPS spectra of Pd-Au NNs/RGO.

Fig. 5. FT-IR (A) and Raman (B) spectra of Pd-Au NNs/RGO (curve a) and GO (curve b).

Fig. 6. CO-stripping cyclic voltammograms of Pd-Au NNs/RGO (A) and Pd black (B) modified GCE in 0.5 M H_2SO_4 at a scan rate of 50 mV s^{-1}.

Fig. 7. (A) LSVs of Pd-Au NNs/RGO (curve a), Pd black (curve b), Pd-C (curve c), modified RDE in oxygen-saturated 0.1 M KOH at a scan rate of 5 mV s^{-1}, using the

rotation rate of 1600 rpm. (B) The corresponding mass activity at –0.1 V. (C) LSVs of Pd-Au NNs/RGO modified RDE with different rotating rates in oxygen-saturated 0.1 M KOH at a scan rate of 5 mV s^{-1} (curve a-f): 100, 400, 900, 1600, 2500, and 3600 rpm. (D) The corresponding K-L plots at different potentials for ORR.

Fig. 8. The ORR polarization curves before and after the accelerated durability test at a scan rate of 5 mV s^{-1}, using a rotation rate of 1600 rpm.

Fig. 9. Chronoamperometric stability test of Pd-Au NNs/RGO (curve a), Pd black (curve b), and Pd-C (curve c) modified electrodes with a rotating rate of 1600 rpm in oxygen-saturated 0.1 M KOH at the half-wave potential.

Figures

Fig. 1

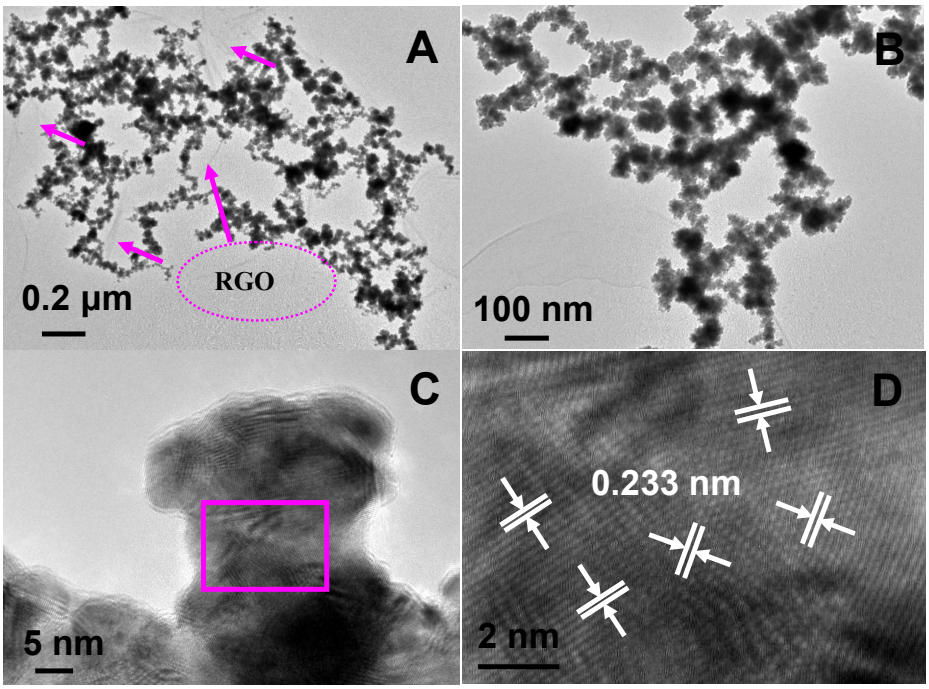

Fig. 2

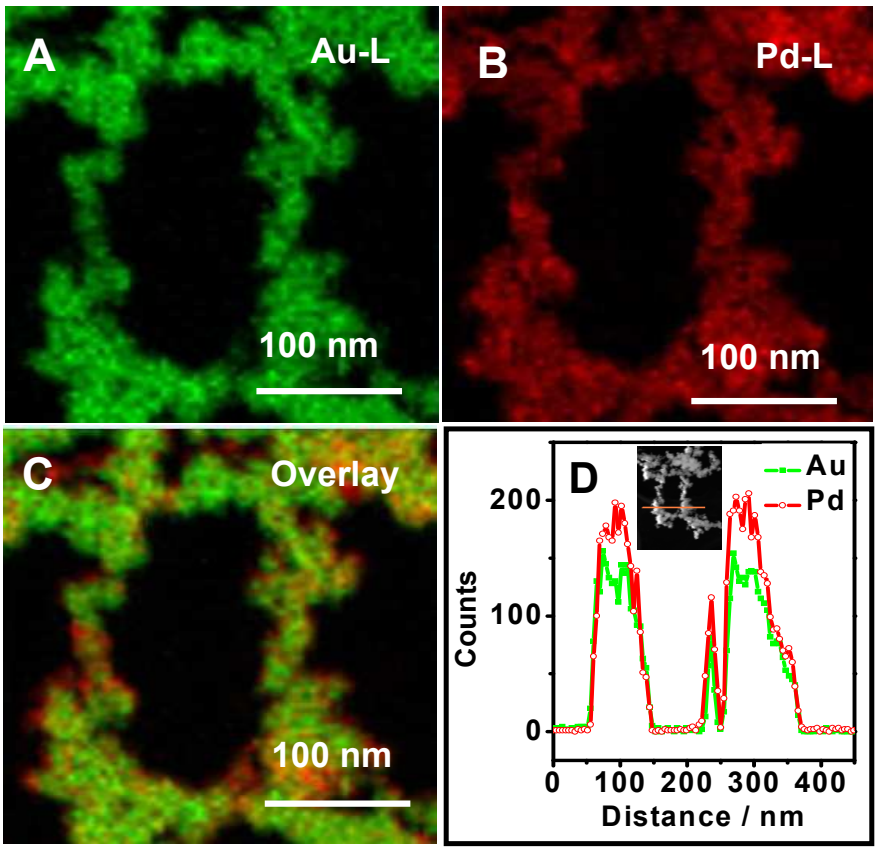

Fig. 3

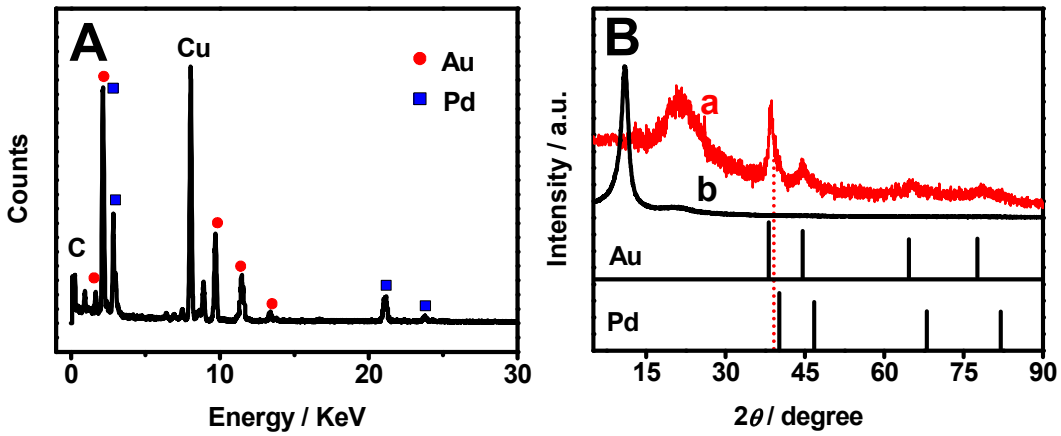

Fig. 4

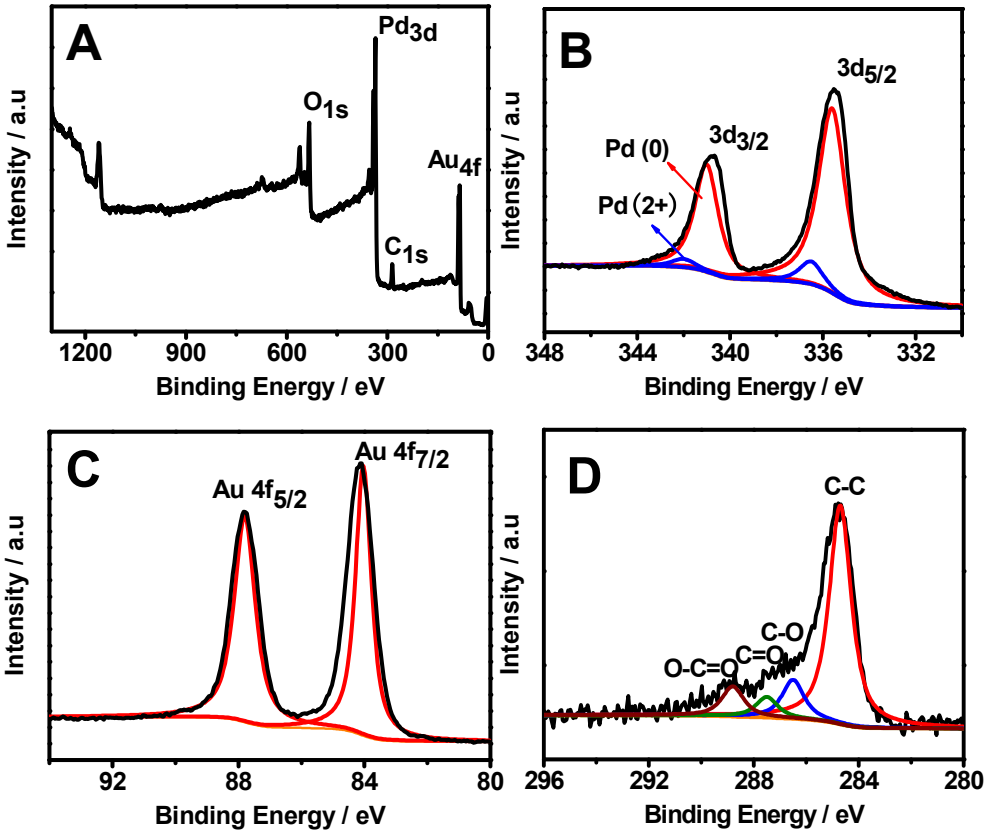

Fig. 5

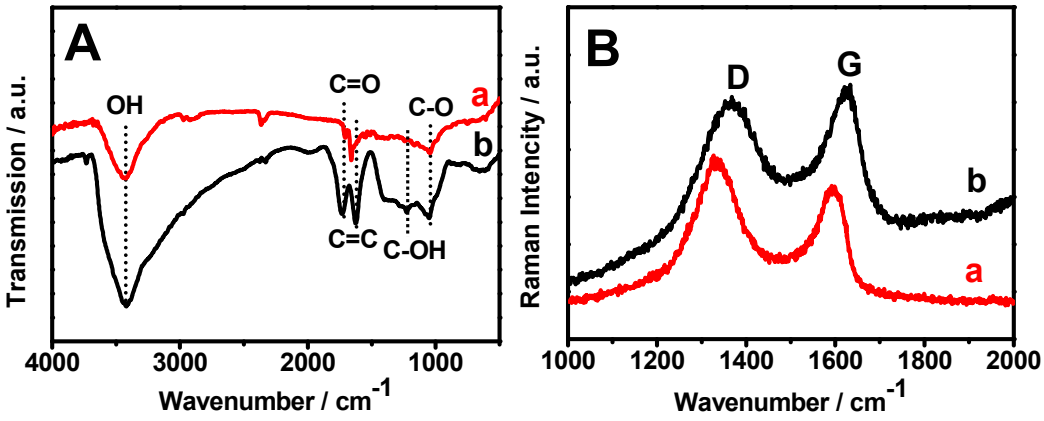

Fig. 6

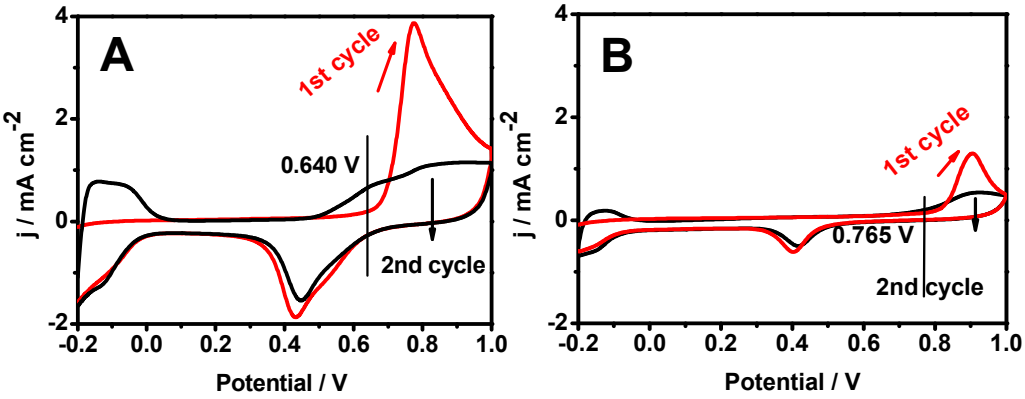

Fig. 7

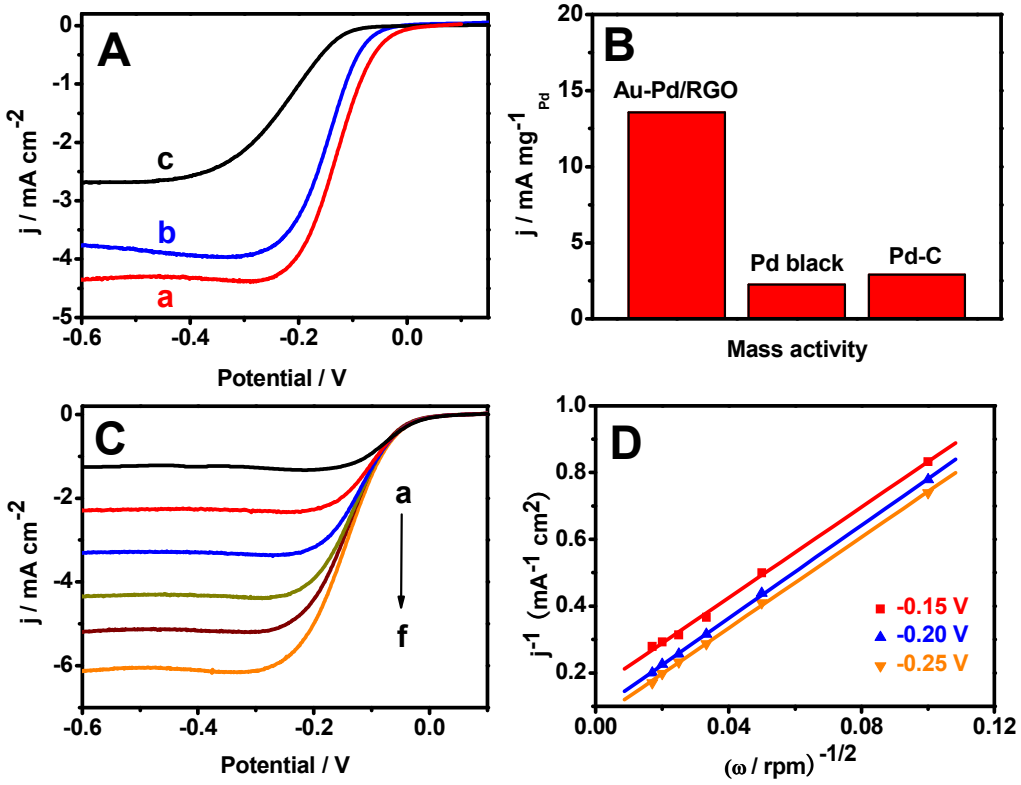

Fig. 8

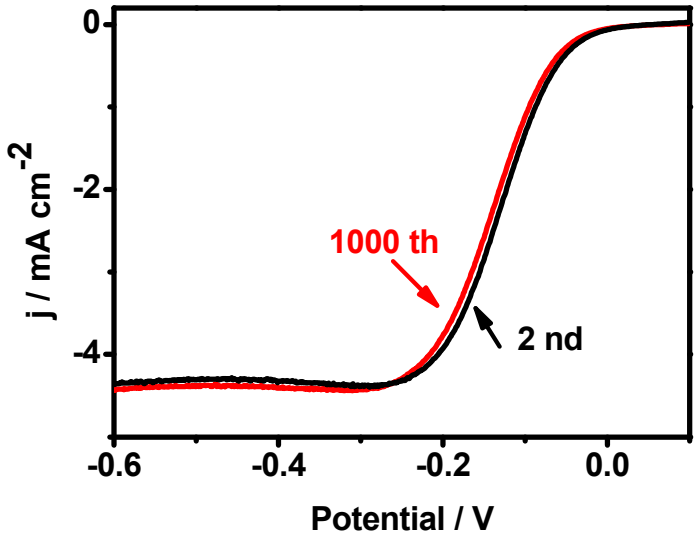

Fig. 9